Chapter 4

Program PISA-QMS

4.1 Outline of PISA-QMS

We have developed the original computer program PISA-QMS to simulate ion trajectories in RF-QMF and ITMS[7]. There are two options in PISA-QMS. One is suitable for the calculation of ion trajectories in RF-QMF, and the other is aimed at the analysis of the ion motions in ITMS. The main difference between the two is in the calculation of the electric fields. The boundary element method (BEM) is employed for RF-QMF, while the multipole expansion method is adopted for ITMS as described later.

For an ion with mass m and charge q, the equation of ion motion in PISA-QMS is taken to be

$$m\frac{d^2u(t)}{dt^2} = q\left(E_{q,u} + E_{res,u}\right) + F_{r,u} + F_{s,u} \qquad (u=x, y, \text{ or } z). \qquad (4.1.1)$$

The first term of the right-hand side of this equation represents the electric forces in the ion transmitting or the ion trapping field $E_{q,u}$. In the second term, $E_{res,u}$ is the field which is applied to the end-cap electrodes of ITMS for ion extraction. The third term $F_{r,u}$ expresses the effective macroscopic damping force which is derived by approximating the microscopic process of collisions with ion-buffering gas atoms. The fourth term $F_{s,u}$ represents the force given to ions by the space charge confined in a limited space around the center of ITMS. For simulations of ion trajectories in RF-QMF, only the first term is considered because the ion extraction field $E_{res,u}$ is not required. Since ion buffering gas is not necessary for RF-QMF, the terms of $F_{r,u}$ and $F_{s,u}$ may also be dropped.

The program PISA-QMS calculates ion motions in RF-QMF or ITMS point by point in the space at corresponding times. A typical sequence of calculations is as follows.

1. The calculation of the electric field in accordance with a given electrode configuration.
2. The input of the initial position, initial velocity, initial phase of RF voltage, m and charge q of an ion.
3. The numerical integration of the equation of ion motion to obtain the position $u_1(\Delta t)$ and velocity $\dot{u}_1(\Delta t)$ after the movement of the ion for the short time Δt.
4. The calculation of the new value of electric field at the position of $u_1(\Delta t)$ and the time $t = \Delta t$ taking into account that the electric field varies with time.
5. The numerical integration of the equation of ion motion to obtain the new position $u_2(\Delta t)$ and velocity $\dot{u}_2(\Delta t)$ after the next short time Δt.
6. Repetition of the calculation of items 4 and 5.

The ion trajectory is obtained as a series of solutions u_1, u_2, u_3, $\cdots$. This trajectory is different from the solution of the Mathieu equation which is a linear combination of sinusoidal functions. The solution of the Mathieu equation is not used in our program PISQA-QMS.

PISA-QMS can be divided into the following three parts: (1) the calculation of electric fields; (2) the calculation of ion trajectories; and (3) the calculation of the interactions of ions with carrier gas atoms and space charge. Flow charts of the two calculation options are shown in Figs. 4-1(a) and (b). The details of each part are described below.

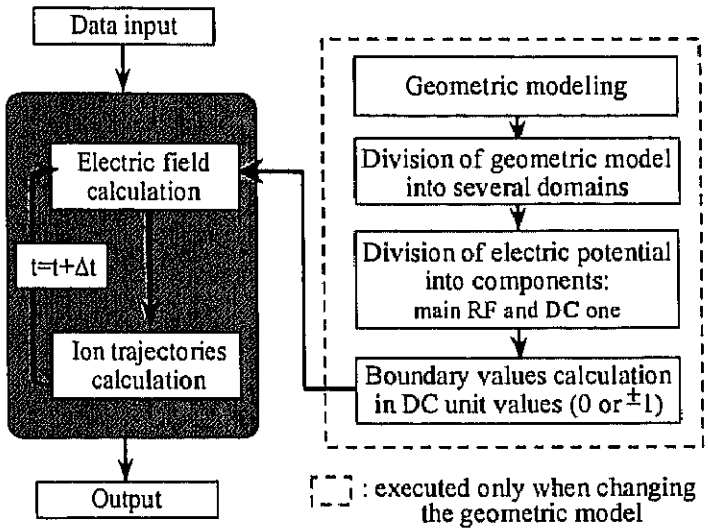

Fig.4-1(a) Calculation flow chart for RF-QMF. The portion within the dashed lines is executed only once.

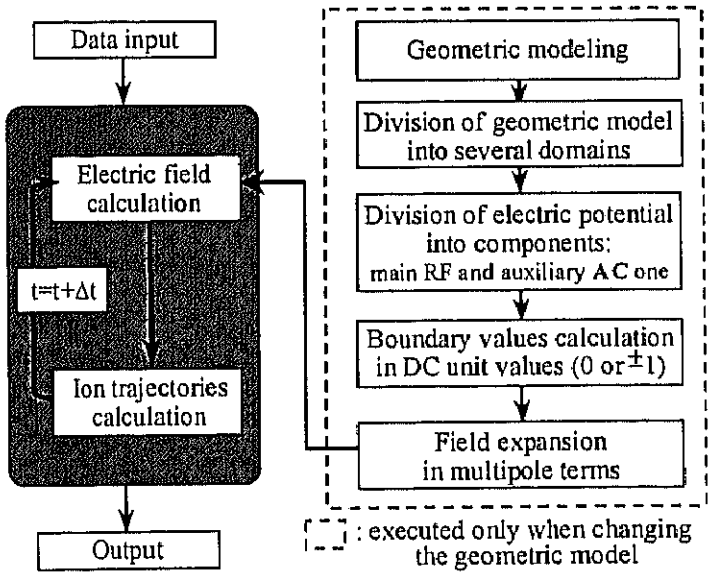

Fig.4-1(b) Calculation flow chart for ITMS. The portion within the dashed lines is executed only once.

4.2 Calculation of electric fields

4.2.1 Boundary element method

High accuracy of the positioning of four rods in the mechanical construction is required especially in RF-QMF to obtain high mass resolution. The positioning error must be at least within 2-3 μm to achieve a mass resolution of $m/\Delta m$=2000. In order to evaluate the effect of such a low positioning error, the electric fields generated with practical electrodes must be calculated with a numerical error as low as 0.01 %. In PISA-QMS, BEM is adopted for the calculation of electric fields in RF-QMF with high numerical accuracy.

The electric field in a charge-free space is derived from the potential Φ which satisfies the Laplace equation:

$$\nabla^2\Phi = 0 \ . \qquad (4.2.1)$$

We introduce a certain volume Λ, and consider the potential Φ in this volume. We express the boundary surface by Γ. A schematic drawing of the volume Λ with its boundary surface Γ is described two dimensionally in Fig.4-2.

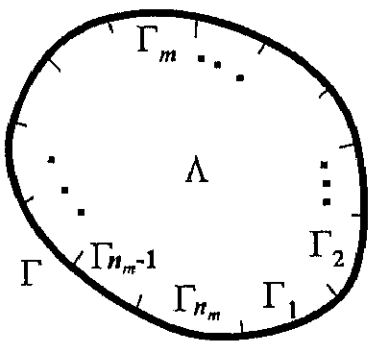

Fig.4-2 A schematic drawing of the volume Λ. The volume is surrounded by boundary Γ. The boundary Γ is divided into small elements from Γ_1 to Γ_{n_m}.

Using Green's theorem, the potential Φ_i at the source point i in Λ is given by the following boundary integrals:

$$C_i\Phi_i + \int_\Gamma \Phi_b \left(\frac{\partial \Phi^*}{\partial n}\right)_b d\Gamma = \int_\Gamma \Phi^*{}_b \left(\frac{\partial \Phi}{\partial n}\right)_b d\Gamma \qquad (4.2.2)$$

where Φ^* is such a known fundamental solution of eq.(4.2.1) as $1/(4\pi r)$. The symbol C_i is a constant that depends on the solid angle subtended by Γ at the point i [28]. The eq.(4.2.2) implies that for the charge-free volume Λ the potential Φ_i anywhere inside Λ can be calculated from the potential value Φ_b and the normal derivative $(\partial\Phi/\partial n)_b$ on the boundary surface Γ only. This is a basic equation of the BEM. Therefore, all unknown values (Φ_b or $(\partial\Phi/\partial n)_b$) need to be solved by using eq.(4.2.2) when the source point i is on the boundary Γ. The method to solve all the boundary values by BEM is described below.

In the application of this BEM to practical problems, it is convenient to divide the boundary surface Γ into several elements. Denoting the number of surface elements by n_m as shown in.Fig.4-2, we write eq.(4.2.2) as

$$C_i\Phi_i + \sum_{m=1}^{n_m} \int_{\Gamma_m} \Phi_b \left(\frac{\partial \Phi^*}{\partial n}\right)_b d\Gamma_m = \sum_{m=1}^{n_m} \int_{\Gamma_m} \Phi^*{}_b \left(\frac{\partial \Phi}{\partial n}\right)_b d\Gamma_m \qquad (4.2.3)$$

with

$$\Gamma = \sum_{m=1}^{n_m} \Gamma_m \,. \qquad (4.2.4)$$

In accordance with the division of the surface Γ into n_m elements, Φ_b, $(\partial\Phi/\partial n)_b$ and coordinates u (u=x, y, or z) on each surface element can be expressed in the following forms:

$$\Phi_b = \sum_{k'=1}^{n_{k'}} \varphi_{k'}(\xi_1, \xi_2) \cdot \Phi^b_{k'} \,, \qquad (4.2.5)$$

$$\left(\frac{\partial \Phi}{\partial n}\right)_b = \sum_{k'=1}^{n_{k'}} \varphi_{k'}(\xi_1, \xi_2) \cdot \left(\frac{\partial \Phi}{\partial n}\right)^b_{k'} \qquad (4.2.6)$$

and

$$u = \sum_{k=1}^{n_k} \varphi_k(\xi_1, \xi_2) \cdot u_k \tag{4.2.7}$$

where ξ_1 and ξ_2, varying from −1 to +1, are local cartesian coordinates on each element as shown in Table 4-1, instead of using x and y coordinates. In these expressions, $\varphi_{k'}$, $\varphi_{k''}$ and φ_k are functions that interpolate the potential Φ_b, the normal derivative $(\partial\Phi/\partial n)_b$ and the shape of each element on the boundary surface Γ, respectively. The suffixes k', k'' and k of the interpolation functions, $\varphi_{k'}$, $\varphi_{k''}$ and φ_k, mean nodal points on each element. At each nodal point, the potential, its normal derivative and the position coordinate are denoted by $\Phi_{k'}{}^b$, $(\partial\Phi/\partial n)_{k''}{}^b$ and u_k. The nodal points are determined according to the order of the interpolation function. Table 4-1 shows linear and quadratic interpolation functions with nodal points in a boundary element. Usually the order of functions for interpolation of the potential is unified in all elements. The functions for interpolation of the normal derivative and the shape of each element are defined in the same way. In order to minimize the memory size needed for calculations, the order of the functions for interpolation is determined in each element in our method. For example, for calculation of the potential in the space between two coaxial cylindrical electrodes (see the surfaces A, B, C and D of Fig.4-6, Subsection 4.2.3), quadratic functions are taken for the elements on curved surfaces A and B, while linear functions are chosen for the elements on linear surfaces C and D. The electric potential value Φ_b and the normal derivative $(\partial\Phi/\partial n)_b$ can be determined in the same manner.

Table 4-1. Linear and quadratic interpolation functions with nodal points in a boundary element

	Element	
	Linear	Quadratic
Nodal points	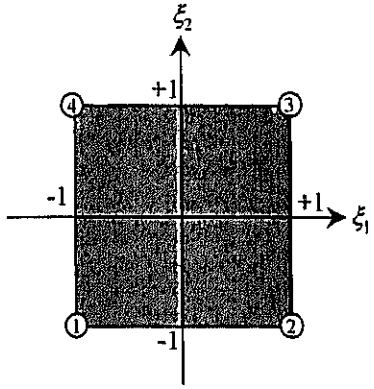	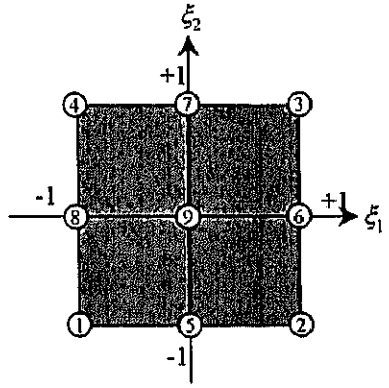
Interpolation functions	$\varphi_1=\frac{1}{4}(1-\xi_1)(1-\xi_2)$ $\varphi_2=\frac{1}{4}(1+\xi_1)(1-\xi_2)$ $\varphi_3=\frac{1}{4}(1+\xi_1)(1+\xi_2)$ $\varphi_4=\frac{1}{4}(1-\xi_1)(1+\xi_2)$	$\varphi_1=\frac{1}{4}\xi_1\xi_2(1-\xi_1)(1-\xi_2)$ $\varphi_2=-\frac{1}{4}\xi_1\xi_2(1+\xi_1)(1-\xi_2)$ $\varphi_3=\frac{1}{4}\xi_1\xi_2(1+\xi_1)(1+\xi_2)$ $\varphi_4=-\frac{1}{4}\xi_1\xi_2(1-\xi_1)(1+\xi_2)$ $\varphi_5=-\frac{1}{2}\xi_2(1+\xi_1^2)(1-\xi_2)$ $\varphi_6=\frac{1}{2}\xi_1(1+\xi_1)(1-\xi_2^2)$ $\varphi_7=\frac{1}{2}\xi_2(1+\xi_1^2)(1+\xi_2)$ $\varphi_8=-\frac{1}{2}\xi_1(1-\xi_1)(1-\xi_1^2)$ $\varphi_9=(1-\xi_1^2)(1-\xi_1^2)$

From eqs.(4.2.5), (4.2.6) and (4.2.7), integration within each element Γ_m in eq.(4.2.3) are rewritten as follows:

$$\int_{\Gamma_m}\Phi_b\left(\frac{\partial\Phi^*}{\partial n}\right)_b d\Gamma_m=\sum_{k'=1}^{n_m}\Phi_{k'}^b\int_{-1}^{+1}\varphi_{k'}(\xi_1,\xi_2)\left(\frac{\partial\Phi^*(\xi_1,\xi_2)}{\partial n}\right)|\,G(\xi_1,\xi_2)\,|\,d\xi_1 d\xi_2 \qquad (4.2.8)$$

$$\int_{\Gamma_m}\Phi_b{}^*\left(\frac{\partial\Phi}{\partial n}\right)_b d\Gamma_m=\sum_{k'=1}^{n_m}\left(\frac{\partial\Phi}{\partial n}\right)_{k'}^b\int_{-1}^{+1}\varphi_{k'}(\xi_1,\xi_2)\,\Phi^*(\xi_1,\xi_2)\,|\,G(\xi_1,\xi_2)\,|\,d\xi_1 d\xi_2 \qquad (4.2.9)$$

where $|G((\xi_1,\ \xi_2))|$ is a Jacobian due to transformation of the coordinate system from the global coordinate system (x, y, z) to the local coordinate system $(\xi_1,\ \xi_2)$ within each element as shown in Table 4-1.

Substituting eqs.(4.2.8) and (4.2.9) into eq.(4.2.3), and rearranging the number of nodal points j from 1 to N, that is the total number of nodal points on the whole boundary Γ, we replace eq.(4.2.3) by the following algebraic equation:

$$\sum_{j=1}^{N} H_{ij}\Phi_j^b = \sum_{j=1}^{N} G_{ij}\left(\frac{\partial\Phi}{\partial n}\right)_j^b \tag{4.2.10}$$

where Φ_j^b and $(\partial\Phi/\partial n)_j^b$ denote the boundary potential value and its normal derivative value at nodal point j, respectively. The coefficients H_{ij} and G_{ij} are given in the following integral forms:

$$H_{ij} = \mathrm{C}_i\delta_{ij} + \int_{-1}^{+1}\varphi_j(\xi_1,\xi_2)\left(\frac{\partial\Phi^*(\xi_1,\xi_2)}{\partial n}\right)|\,\mathrm{G}(\xi_1,\xi_2)\,|\,d\xi_1 d\xi_2 \tag{4.2.11}$$

and

$$G_{ij} = \int_{-1}^{+1}\varphi_j(\xi_1,\xi_2)\Phi^*(\xi_1,\xi_2)\,|\,\mathrm{G}(\xi_1,\xi_2)\,|\,d\xi_1 d\xi_2\,. \tag{4.2.12}$$

When potential value Φ_j^b is given as a known boundary value at nodal point j, the value of $(\partial\Phi/\partial n)_j^b$ is unknown. Similarly, when $(\partial\Phi/\partial n)_j^b$ is known, Φ_j^b is unknown. Since the number of unknown values included in eq.(4.2.10) is N, that is equal to the number of known values, N simultaneous equations are required to solve all unknown boundary values. Therefore, by setting the source point i to every nodal point j ($1 \le j \le N$), the following simultaneous equations are obtained.

$$\sum_{i=1}^{n}\sum_{j=1}^{n} H_{ij}\Phi_j^b = \sum_{i=1}^{n}\sum_{j=1}^{n} G_{ij}\left(\frac{\partial\Phi}{\partial n}\right)_j^b \tag{4.2.13}$$

The calculation of H_{ij} and G_{ij} is carried out using the Gauss-Legendre integration formula[29] except when the point i coincides with node j in each element. In that case, we employ a polar coordinate integration scheme which was developed by Koizumi and Utamura[30] to improve numerical accuracy for improper integration by modifying the Gauss-Legendre integration formula. Thus, the values of all the unknown boundary values of Φ_j^b or $(\partial\Phi/\partial n)_j^b$ are obtained

by solving eq.(4.2.13). From eqs.(4.2.3) and (4.2.10), unknown potential values ϕ_i inside the space surrounded by four electrodes (in the volume Λ) are finally calculated using all known boundary values Φ_j^b and $(\partial\Phi/\partial n)_j^b$ as follows:

$$\phi_i = \sum_{j=1}^{N} G_{ij}\left(\frac{\partial\Phi}{\partial n}\right)_j^b - \sum_{j=1}^{N} H_{ij}\Phi_j^b . \qquad (4.2.14)$$

The input parameters to initiate the calculation are the potential and normal derivatives which are known by the boundary conditions. Instead of the input of practical potential values on electrodes like $U\text{-}V_{RF}\cos\Omega t$, unit values of ± 1 are given to eq.(4.2.13) as known boundary values. This means that we put $\pm\Phi_0 = \pm 1$ in eq.(3.2.1) and Fig.3-2 in Subsection 3.2.1. Then all unknown potential values in the space surrounded by four electrodes (in the volume Λ) are solved in fractions $\phi_i<1$ of the unit values. Once all unknown boundary values are solved, the electric potential $\Phi(x,y,z;t)$ at any time and position in the volume Λ is obtained by multiplying the fractions by the practical potential values, namely

$$\Phi(x,y,z;t) = \Phi_0 \cdot \phi_{ij} = (U - V_{RF}\cos\Omega t)\cdot\phi_{ij} . \qquad (4.2.15)$$

From this potential, the electric field can be derived as follows:

$$E_{u,ij} = -\frac{\partial\Phi(x,y;t)}{\partial u} = -\frac{\partial}{\partial u}\left\{\phi_{ij}\left(U - V_{RF}\cos\Omega t\right)\right\} \quad (u = x \text{ or } y). \qquad (4.2.16)$$

The use of the unit values mentioned above is very advantageous to shorten the time for ion trajectory calculations, because the calculation of the electric field is finished just once for a given electrode configuration.

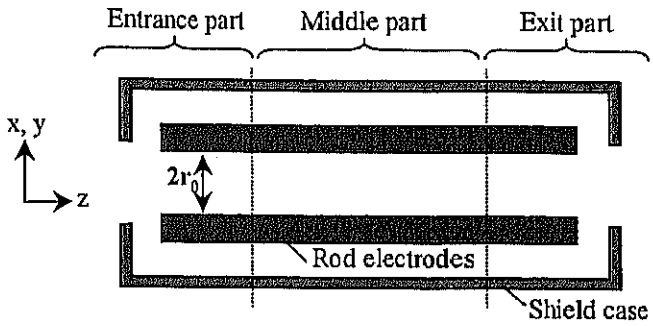

Fig.4-3 Division of the space for calculations for RF-QMF.

In order to save computer memory and computing time further, PISA-QMS is able to divide the space for calculations into several subspaces. In the case of RF-QMF, for example, the space for calculations can be divided into the entrance, the middle and the exit parts as depicted in Fig.4-3. The fields in the entrance and exit parts are calculated using the three-dimensional method, and ion trajectories are obtained from calculations of ion motions in those fields. Hence, the effect of the fringing field at the entrance and the exit of the four rod electrodes is only included. The field in the middle part is calculated with the two-dimensional method. This reduction of the number of dimensions shortens computing time and uses a rather small area of memory as compared to the case where three-dimensional calculations are performed over the whole space of the mass spectrometer. No problem takes place in the connection of ion trajectories computed for each part separately. Fig.4-4 shows ion trajectories obtained in this way.

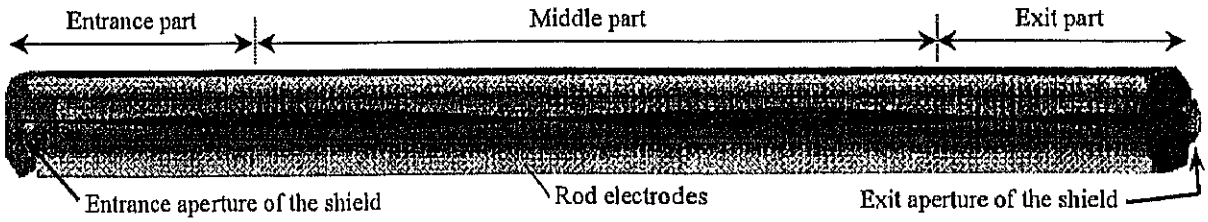

Fig.4-4 Total trajectories of the 85u ions obtained by linking the trajectories calculated in each part. The values of a and q were taken to be 0.2363 and 0.706. The focal position was assumed to be just at the edge of the rod electrodes.

4.2.2 Multipole expansion method

Calculation of the electric field in ITMS does not require as high an accuracy as numerical calculations in RF-QMF, since a small distortion of the field is no longer the principal factor which deteriorates the performances. The deviation of the electrode shape from the ideal one or misalignment of the ring electrode relative to the end-cap electrodes in their mechanical construction, however, brings about multipole fields other than the quadrupole field. The ideal quadrupole field increases linearly with the ion position as shown in eqs.(3.3.9) and (3.3.10). On the other hand, multipole fields other than the quadrupole one are called *nonlinear multipole fields* because such fields no longer have a linear relationship with the ion position. Nonlinear multipole fields have been regarded as having a bad effect on ITMS performance. It was reported that influence of nonlinear multipole fields was such as to deteriorate ion storage and to cause undesirable ion losses[31,32]. More recently, however, the beneficial influence of weak nonlinear multipoles on mass resolution and ion motion stability has become more widely known[33]. Therefore, it is important to include the influence of the nonlinear multipole fields when estimating actual performance.

The electric potential Φ in ITMS can be divided into two components, the potential for ion trapping Φ_{trap} and the potential for ion resonating Φ_{res} as shown in Fig.4-1(b)[10,34]. The former is produced by the trapping RF voltage applied on the ring electrode, whereas the latter is by the auxiliary RF voltage application across two end-cap electrodes. The electric potential in ITMS is expressed in the form of a multipole expansion given by eq.(3.3.2). Here we write it in a slightly modified form by normalizing the radial coordinate r_p by r_0 which is the inner radius of the ring electrode. The explicit form is

$$\Phi(\rho,\theta) = \Phi_0 \sum_{n=0}^{\infty} A_n' \frac{\rho^n}{r_0^n} P_n(\cos\theta) = \Phi_0 \sum_{n=0}^{\infty} C_n \Phi_n \qquad (4.2.17)$$

where

$$C_n = \frac{A_n'}{r_0^{\,n}} \qquad \text{and} \qquad \Phi_n = \rho^n P_n(\cos\theta).$$

Here the symbol Φ_0 indicates $V_{RF}\cos\Omega t$ in the case of $\Phi=\Phi_{trap}$, or $V_{res}\cos\omega_{res}t$ in the case of $\Phi=\Phi_{res}$. Thus, the electric potential Φ can be expanded in $2n$-pole multipole terms from $n=0$ to $n=\infty$. In practice, expansion of the electric potential Φ is taken up to the multipole term of a finite order of N. Therefore, eq.(4.2.17) is rewritten as

$$\Phi(\rho,\theta) = \Phi_0\phi_0 = \Phi_0\sum_{n=0}^{N} A_n' \frac{\rho^n}{r_0^{\,n}} P_n(\cos\theta) = \Phi_0\sum_{n=0}^{N} C_n\Phi_n \qquad (4.2.18)$$

where

$$\phi_0 = \sum_{n=0}^{N} C_n\Phi_n .$$

Here the symbol ϕ_0 denotes the fractional potential when $\Phi(\rho,\theta)$ is normalized to unity. The calculation of coefficients C_n for multipole order of $2n$ can be performed for $\phi_{0,\,trap}$ or $\phi_{0,\,res}$ separately so as to obtain $C_{n,trap}$ or $C_{n,res}$. In the same manner as for RF-QMF, the electric potential Φ_{trap} is solved in fractions $\phi_{0,\,trap}$ by the BEM by giving unit values of +1 to the ring electrode. The potentials of the end-cap electrodes are put to null as shown in Fig. 4-5(a). Once the fractions $\phi_{0,\,trap}$ are obtained, the potential at any position and time is given by multiplying the actual voltage $\Phi_{0,\,trap}$ as follows:

$$\Phi_{trap}(\rho,\theta;t) = \Phi_{0,trap}\phi_{0,trap} = (V_{RF}\cos\Omega t)\sum_{n=0}^{N} C_{n,trap}\Phi_n . \qquad (4.2.19)$$

The electric potential Φ_{res} is solved in fractions $\phi_{0,\,res}$ by giving unit values of ± 1 to the end-cap electrodes as shown in Fig. 4-5(b). The potential of the ring electrode is put to null. Thus the potential Φ_{res} at any position and time is given by

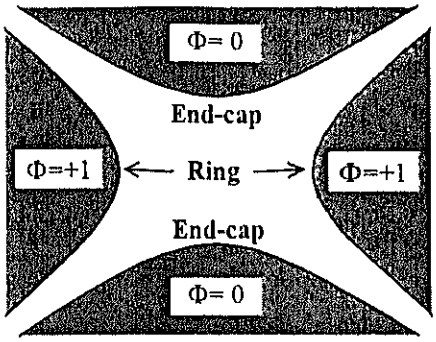

Fig.4-5(a) The method to give unit boundary values to solve the electric potential for ion trapping Φ_{trap}. Unit value +1 is given to the ring electrode, while the two end-cap electrodes are earthed.

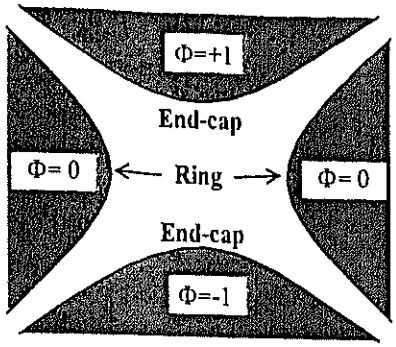

Fig.4-5(b) The method to give unit boundary values to solve the electric potential for ion resonance Φ_{res}. Unit values +1 and -1 are given to the two end-cap electrodes, respectively, while the ring electrode is earthed.

$$\Phi_{res}(\rho,\theta;t) = \Phi_{0,res}\phi_{0,res} = (V_{res}\cos\omega_{res}t)\sum_{n=0}^{N} C_{n,res}\Phi_n . \qquad (4.2.20)$$

The electric fields are easily derived from the above potentials. It is more convenient to write the electric fields in terms of the fractional potentials obtained for unit potentials. The z-component is for instance given by

$$\varepsilon_{z,trap} = -\frac{\partial\phi_{0,trap}}{\partial z} = \sum_{n=0}^{N} C_{n,trap}\left(-\frac{\partial\Phi_n}{\partial z}\right) = \sum_{n=0}^{N} C_{n,trap}(E_n)_z \qquad (4.2.21)$$

and

$$\varepsilon_{z,res} = -\frac{\partial\phi_{0,res}}{\partial z} = \sum_{n=0}^{N} C_{n,res}\left(-\frac{\partial\Phi_n}{\partial z}\right) = \sum_{n=0}^{N} C_{n,res}(E_n)_z . \qquad (4.2.22)$$

The electric field for calculations of ion trajectories can simply be written as

$$E_{z,trap} + E_{z,res} = \varepsilon_{z,trap}\cdot V_{RF}\cos\Omega t + \varepsilon_{z,res}\cdot V_{res}\cos\omega_{res}t . \qquad (4.2.23)$$

In this way, the calculation of the electric field is finished just once for a given electrode configuration in the case of ITMS also. Both electric fields of $E_{z,trap}$ and $E_{z,res}$ at any ion position can be obtained by just multiplying the applied voltages every time step Δt. The time needed for

the calculation of ion trajectories is greatly reduced by using the unit boundary values of potentials.

4.2.3 Accuracy of numerical calculations

The accuracy of calculations of electric fields by means of PISA-QMS was tested in the electrode configuration shown in Fig.4-5(a). The volume Λ was defined by two coaxially-placed tube electrodes and two planes perpendicular to the tube axis. The boundary of the volume Λ was subdivided into A, B, C and D surfaces as indicated in Fig.4-5.

The electric field in Λ was calculated for the following three cases, in each of which the interpolation functions, shown in Table 4-1, were employed differently.

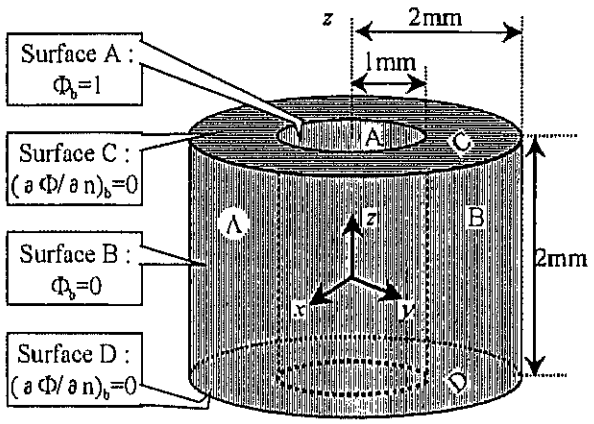

Fig.4-6(a) The boundary of the volume Λ and the boundary conditions used for the test calculation. The boundary conditions were as follows: surface A, Dirichlet condition (Φ_b=1); surface B, Dirichlet condition (Φ_b=0); surfaces C and D, Neumann condition ($(\partial\Phi/\partial n=0)_b$).

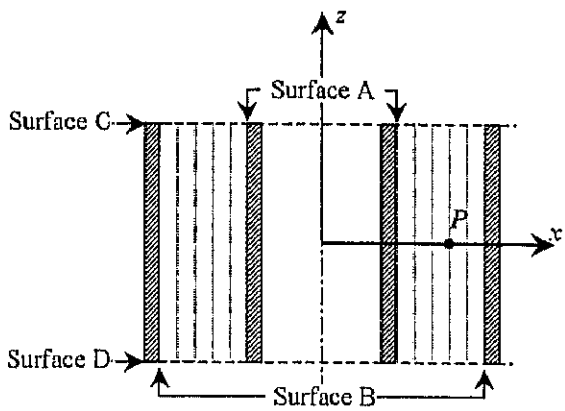

Fig.4-6(b) The electric potential distribution obtained by calculation. The equipotential lines are denoted by dotted lines. At the inner point *P* the electric fields obtained by calculation and by the strict solution are compared.

Case 1. A linear function was adopted to interpolate potential distributions on all the surface elements.

Case 2. The linear function in case 1 was replaced by a quadratic function.

Case 3. The quadratic function was applied to the elements on the surfaces C and D, while the linear function was used for the elements on the surfaces A and B.

As the boundary values, the electric potentials Φ_b=1 and 0 were given to the elements on surfaces A and B, while the normal derivative $(\partial\Phi/\partial n)_b$ =0 was given to the elements on surfaces C and D. The boundary condition in which Φ_b was given as the boundary value is called the Dirichlet condition, while the boundary condition, in which the boundary value $(\partial\Phi/\partial n)_b$ =0 was given, is called the Neumann condition. The Neumann condition $(\partial\Phi/\partial n)_b$ =0 means that distribution of the electric potential is symmetrical with respect to the plane of the surface. Fig.4-5(b) shows the electric potential distribution in volume Λ between the two coaxially-placed tube electrodes as shown in Fig.4-5(a). The electric potential seems to be distributed uniformly even for the space close to surfaces C and D which employ the Neumann condition. Therefore, the electric field obtained by our modified BEM can be compared with the strict solutions.

The strict electric field in the volume Λ between the two tube electrodes, the radii of which are r_1 and r_2 ($r_1 < r_2$), is given by

$$E_r = \frac{(V_1 - V_2)}{ln(r_2/r_1)} \cdot \frac{1}{r} \tag{4.2.24}$$

where V_1 and V_2 are electric potentials on the inner and outer tube electrodes, respectively. In general, numerical errors become bigger as the inner source point i inside Λ comes close to the boundary. However, ions usually transmit or oscillate in the middle of the volume Λ. The middle point P of the volume Λ was chosen to test the numerical accuracy of the electric field. At the point (x, y, z)=(1.5mm, 0, 0) marked P in Fig.4-6(b) the errors of the calculated electric field

relative to the exact field is compared in Fig.4-7 for the above three cases. The errors of the calculation in case 3 are almost equal to those in case 2, but much smaller than those in case 1. The relative errors in case 3 become less than 0.01 %, if we divide the surfaces into 500 elements. The relative errors become bigger as the inner point P comes close to the boundary. This accuracy of the calculation is fully adequate for evaluating the deterioration of performance caused by 2-3μm positioning errors of the four rod electrodes in QMF.

Fig.4-8 indicates the memory size needed for calculations of the above three cases. The size in case 3 is about 60 % of that in case 2. The time necessary for the calculation in case 3 is about 80 % of that in case 2. Since this calculation volume Λ is very simple, the actual calculation times were 1 to 4 minutes using the supercomputer HITAC S-820. As the electrodes configuration becomes more complex, such reduction of calculation time becomes more important. It is evident that the modified BEM employed in PISA-QMS is very advantageous to achieve high accuracy of calculations with a smaller memory size and shorter computing time.

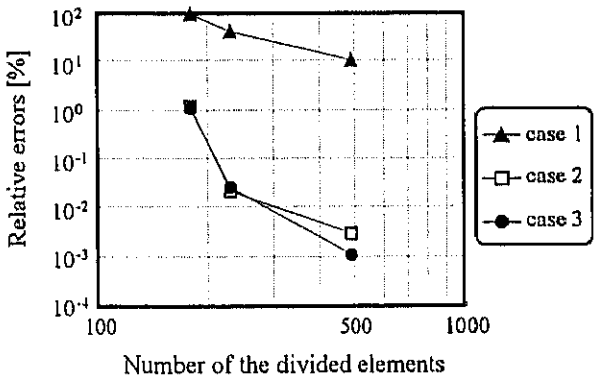

Fig.4-7 Comparison of relative error versus number of divided elements for three cases. The interpolative function of potential was selected as follows: case 1, linear; case 2, quadratic; case 3, linear or quadratic.

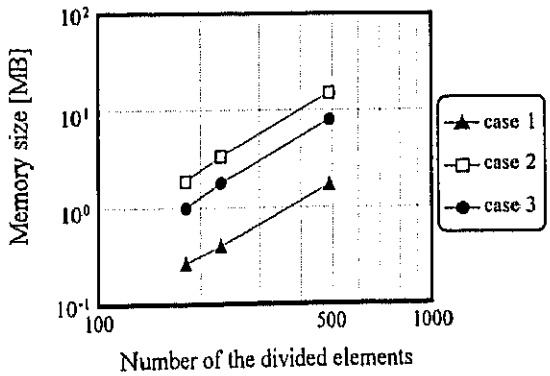

Fig.4-8 Comparison of memory size needed for the test calculation versus number of divided elements for three cases.

4.3 Calculation of ion motions

4.3.1 The Shanks method

Ion trajectories are calculated by integrating the equation of ion motion given by eq.(4.1.1). There are several numerical integration methods for ordinary differential equations. In any method the electric field must be evaluated at every ion position and time step, since ions are moving in space with time. Most of the computing time is spent for calculation of the electric field. A small number of times to make the electric field calculation is, therefore, desirable for rapid computations.

In our program PISA-QMS, we adopted the Shanks method for the integration of eq.(4.1.1) to obtain ion trajectories[35]. This method is an 8th-order Runge-Kutta method, and it is often used for calculation of artificial satellite orbits. This choice of integration method was based on preliminary calculations of ion trajectories in RF-QMF with an ideal quadrupole field using Newmark's β–parameter method[36] and the 4th-order Runge-Kutta method[37] as well as the Shanks method. Newmark's β–parameter method is usually employed for vibration problems. The 4th-order Runge-Kutta method is useful for problems in a wide variety of research fields. The calculated ion trajectories in the x-z plane using the theoretical electric field expressed in eq.(3.2.3a) when a_x and q_x values were 0.234 and 0.7044 are displayed in Fig.4-9. The condition was set that the number of times to make the electric field calculation was 1000. The trajectory displayed in (d) in Fig.4-9 is obtained from direct calculation of the stable solution of the Mathieu equation from eqs.(3.2.10) and (3.2.11). We call this the "exact" trajectory. It is obvious from Fig.4-9 that Shanks method provides the closest ion trajectory to the exact one. Table 4-2 summarizes the minimum number of calculations of the electric field. The criterion for the evaluation of these minimum numbers was that the accuracy of the trajectory is better than a few

μm for typical 20cm long, four rod electrodes in RF-QMF. The Shanks method gives the highest numerical accuracy in spite of having the least number of calculations. The calculation speed using the Shanks method is about 11 times faster than that using the 4th-order Runge-Kutta method, assuming that the computing time is almost proportional to the number of calculations of the electric field.

(a) Trajectory calculated with Newmark's β–parameter method

(b) Trajectory calculated with the 4th-order Runge-Kutta method

(c) Trajectory calculated with Shanks method

(d) Exact trajectory in ideal field obtained by eqs.(3.2.10) and (3.2.11)

Fig.4-9 Comparison between exact and calculated trajectories obtained by three methods. For each case, the number of times the electric field calculation was made was set to be 1000.

Table 4-2

Minimum number of times for to make the electric field calculation with 10 μm numerical accuracy after a 20 cm flight for three cases.

Case	Integration method	Minimum number of electric field calculations
(a)	Newmark's β-parameter	6000
(b)	4th-order Runge-Kutta	8000
(c)	Shanks	700

4.3.2 Interaction of ions with buffering gas atoms

In ITMS a neutral gas like helium is usually introduced into spectrometers to buffer ions or to assist in dissociation of ions into fragments. In order to approximate the microscopic interaction between ions and buffering neutral gas atoms, we employed a viscous model. This choice was based on the assumption that ions interact with buffering gas atoms through elastic collisions in their thermal equilibrium[38]. The microscopic interaction between ions and neutral gas atoms with the viscous model is explained in the following.

When the velocities of an ion and a neutral gas atom are V and v, respectively, the relative velocity is $u = v - V$, the direction of which is assumed to be (θ, ϕ) with respect to V. After these particles collide at the point P which is in the direction (Θ, Φ) from the V - u plane, the relative velocity becomes u' which has the same magnitude as u. The polar coordinate system which is fixed to the plane V - u is shown in Fig.4-10. The impulsive force acting on the ion is given by

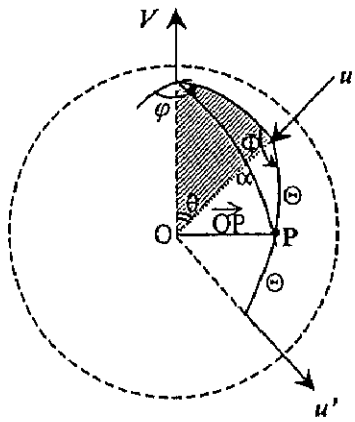

Fig.4-10 The polar coordinate system which is fixed to the shaded plane V - u, where V is velocity of an ion and u is relative velocity between the ion and a neutral gas atom before they collide with each other. With respect to V, u is in the direction (θ, ϕ). After they collide at the point P which is in the direction (Θ, Φ) from the V - u plane, the relative velocity becomes u' which has the same magnitude as u.

$$df_r = -2m_e u\cos\Theta\cos\alpha = -2m_e u\cos\Theta(\cos\theta\cos\Theta + \sin\theta\sin\Theta\cos\Phi) \qquad (4.3.1)$$

where m_e is effective mass and α is the angle between $\overrightarrow{OP}$ and V. Since the effective mass m_e is expressed by

$$m_e = \frac{m \cdot m_b}{m + m_b} \approx m_b, \qquad (4.3.2)$$

eq.(4.3.1) can be approximated as follows:

$$f_r \approx -2m_b u\cos\Theta(\cos\theta\cos\Theta + \sin\theta\sin\Theta\cos\Phi). \qquad (4.3.3)$$

The neutral gas atoms are assumed to be moving in accordance with a Maxwellian velocity distribution. The number of neutral gas atoms per unit volume dn_b which have a velocity between u and $u+du$ within the solid angle (θ, φ) is given by

$$dn_b = n\left(\frac{m_b}{2\pi kT}\right)^{3/2}\exp\left\{-\frac{m_b}{2kT}(u^2 + V^2 - 2uV\cos\theta)\right\}u^2 du\sin\theta d\theta d\varphi \qquad (4.3.4)$$

where n is the neutral gas density, T is its temperature and k is Boltzmann's constant. The volume in which the collision point P is within the solid angle $\sin\Theta d\Theta d\Phi$ per unit time is expressed in the following form:

$$dV = (R+a)^2\sin\Theta d\Theta d\Phi \cdot u\cos\Theta \qquad (4.3.5)$$

where R and a are radii of the ion and the neutral gas atom. Therefore, a damping force acting on ions can be obtained by integrating the multiplication of eqs.(4.3.3), (4.3.4) and (4.3.5) as follows:

$$F_r = \iint f_r dn_b dV$$

$$= -2m_b n\left(\frac{m_b}{2\pi kT}\right)^{3/2}(R+a)^2\int_0^\infty u^4 du\cdot\int_0^\pi 2\pi\sin\theta d\theta\cdot\exp\left\{-\frac{m_b}{2kT}(u^2 + V^2 - 2uV\cos\theta)\right\}$$

$$\times\int_0^{\pi/2}\cos^2\Theta\sin\Theta d\Theta\cdot\int_0^{2\pi} d\Phi(\cos\theta\cos\Theta + \sin\theta\sin\Theta\cos\Phi)$$

$$= -2\pi^2(R+a)^2 n\left(\frac{m_b}{2\pi kT}\right)^{3/2}\frac{(kT)^2}{m_b V^2}$$

$$\times\int_0^\infty u^2\left\{\left(\frac{m_b V}{kT}u-1\right)\cdot\exp\left(-\frac{m_b(u-V)^2}{2kT}\right)+\left(\frac{m_b V}{kT}u+1\right)\cdot\exp\left(-\frac{m_b(u+V)^2}{2kT}\right)\right\}du\,. \tag{4.3.6}$$

Eq.(4.3.6) can be rewritten as follows:

$$F_r = -nkT\pi(R+a)^2\frac{1}{x_0^2}\left\{\frac{2}{\sqrt{\pi}}\int_{-x_0}^\infty (x+x_0)^2(xx_0+x_0^2-1/2)e^{-x^2}dx\right.$$

$$\left.+\frac{2}{\sqrt{\pi}}\int_{+x_0}^\infty (x-x_0)^2(xx_0-x_0^2+1/2)e^{-x^2}dx\right\} \tag{4.3.8}$$

where

$$x=(u\mp V)\sqrt{m_b/(2kT)}$$

and

$$x_0 = V\sqrt{m_b/(2kT)}\,. \tag{4.3.9}$$

Using the following formulas of the integrals of error funtions[39]:

$$\Phi(x_0)=\frac{2}{\sqrt{\pi}}\int_0^{x_0} e^{-x^2}dx\,,$$

$$\frac{2}{\sqrt{\pi}}\int_{\pm x_0}^\infty e^{-x^2}dx = 1\mp\Phi(x_0)\,,$$

$$\frac{2}{\sqrt{\pi}}\int_{\pm x_0}^\infty x\cdot e^{-x^2}dx=\frac{1}{\sqrt{\pi}}e^{-x_0^2}\,,$$

$$\frac{2}{\sqrt{\pi}}\int_{\pm x_0}^\infty x^3\cdot e^{-x^2}dx=\frac{x_0^2+1}{\sqrt{\pi}}\cdot e^{-x_0^2}$$

and

$$\frac{2}{\sqrt{\pi}}\int_{\pm x_0}^\infty x^2\cdot e^{-x^2}dx=\frac{1}{2}\pm\left\{\frac{x_0}{\sqrt{\pi}}e^{-x_0^2}-\frac{1}{2}\Phi(x_0)\right\}\,,$$

we can rewrite eq.(4.3.8) as

$$F_r = -p\pi(R+a)^2\left\{\frac{e^{-x_0^2}}{\sqrt{\pi}x_0}(x+2x_0^2)+(2x_0^2+2-\frac{1}{2x_0^2})\Phi(x_0)\right\} \tag{4.3.10}$$

where p is the neutral gas pressure ($p=nkT$). Assuming that the gas atom's thermal velocity is much higher than the ion velocity V ($x_0<<1$ in eq.(4.3.9)), we can expand $\Phi(x_0)$ as follows:

$$\Phi(x_0)=\frac{2}{\sqrt{\pi}}\left(x_0-\frac{x_0^3}{1!3}+\frac{x_0^5}{2!5}-\ldots\right). \tag{4.3.11}$$

Therefore, from eqs.(4.3.9), (4.3.10) and (4.3.11) the damping force acting on ions can be approximated as follows:

$$F_r=-p\pi(R+a)^2\cdot\frac{16}{3}\sqrt{\frac{m_b}{2\pi kT}}V\left(1+\frac{1}{5}\frac{m_bV^2}{2kT}+\ldots\right)$$

$$\approx -p(R+a)^2\cdot\frac{16}{3}\sqrt{\frac{\pi m_b}{2kT}}V\,. \tag{4.3.12}$$

Thus, a macroscopic coefficient of viscosity is obtained from the calculation of the average probability of collisions of ions with buffering gas atoms which are moving in accordance with the Maxwellian velocity distribution. Since the velocity of ions is not so high, the viscosity is equivalent to a damping force acting on ions in proportion to their velocity.

To examine the effect of the interaction mentioned above, mass spectra were calculated for a ITMS using PISA-QMS. The trajectories of 1620 ions having different initial conditions in ITMS were calculated for operation in the mass-selective instability scan mode with resonance ejection as indicated in Fig.3-11. The parameters used in this simulation are listed in Table 4-3. Mass spectra were obtained from the calculation of ion trajectories in the mass range from 100u to 500u under various pressures of helium gas. Typical results for the mass 300u are shown in Fig.4-11. The shape of the simulated mass spectra fit Gaussian curves to a good approximation. The peak position seems to shift towards the lower mass side as the helium gas pressure goes down.

Table 4-3

ITMS parameters used to simulate mass spectra.

RF Drive voltage (applied to the ring electrode)	
RF frequency (Ω)	909kHz
RF amplitude scan (V_{RF})	72.6-4723 V
Mass range	100-500 u
Resonance AC voltage (applied in dipolar fashion across the end-cap electrodes)	
Resonance AC frequency (ω_{res})	360kHz
Resonance AC amplitude (V_{res})	2.0-5.3 V (0-p)
Resonance ejection condition	q_z=0.859 (β_z=0.792)
Radius of the ring electrode (r_o)	1 *cm*

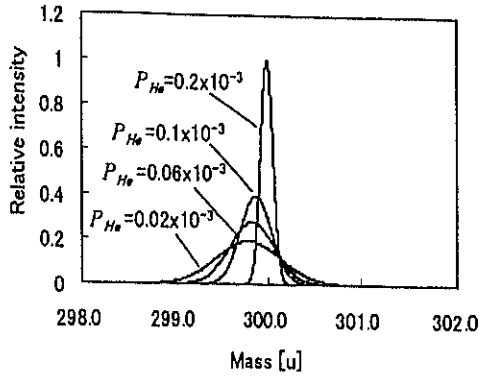

Fig.4-11 Simulated mass spectra of 300 u ions for different He gas pressures, P_{He} [Torr].

Fig.4-12 indicates this mass shift more clearly. As the helium gas pressure increases, the peak position of the mass spectra shifts toward the higher mass side. The mass resolution was evaluated by defining Δm by FWHM of the peak of a mass spectrum. As plotted in Fig. 4-13, Δm decreases rapidly up to a helium gas pressure of 2.0×10^{-4} Torr (2.67×10^{-2} Pa), and then continues in a gradual decrease at higher pressures. In this dissertation, we use "Torr" as a pressure unit, that is conventionally used in most research papers on ITMS. The present simulation predicts that the maximum permissible value of ±0.5 for the mass shift δm and Δm <0.5 for the mass resolution are attained if we operate ITMS with helium gas pressure in the range from 1.0×10^{-4} to 4.0×10^{-4} Torr. This range of helium gas is in good agreement with pressures commonly accepted as optimum operational conditions in experiments[40,41]. Louris *et al.*[40] reported that experiments with ITMS which were performed while maintaining the helium pressure gas at 2.7×10^{-4} Torr inside ITMS. Reiser *et al.*[41] employed helium gas of 1.0×10^{-4} Torr as a standard pressure for their experiments.

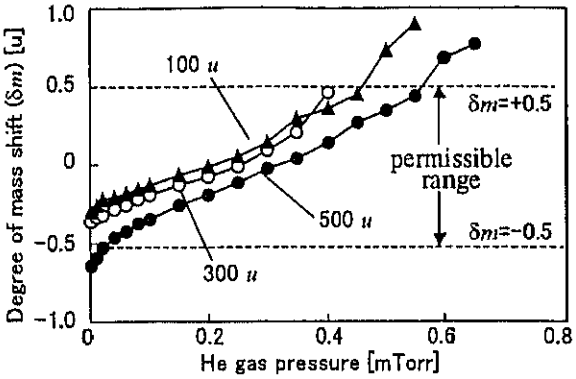

Fig.4-12 The influence of He gas pressure on the degree of mass shift.

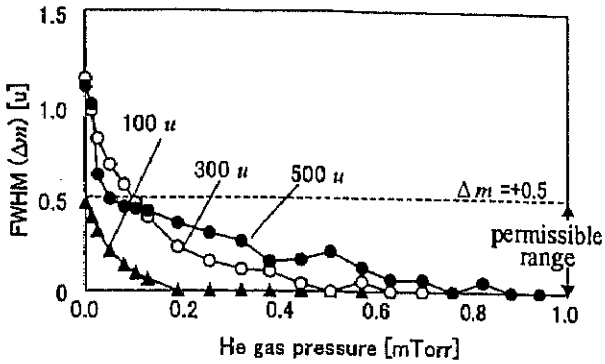

Fig.4-13 The influence of He gas pressure on the value of FWHM.

4.3.3 Ion - space charge interaction

Since all ions are trapped once in the center region of ITMS, it is necessary to take into account the interaction of ions with the space charge. As a space charge model, we assumed a uniformly charged sphere at the center of ITMS. The Coulomb field due to this charge distribution is well known in classical electrodymamics. Denoting the radius and the charge density of the space charge by R_s and ρ_s, respectively, the electric force is written as

$$F_s = q\frac{R_s^3}{3\varepsilon_0}\cdot\frac{1}{r^2}\cdot\frac{r}{r} \quad (r > R_s) \qquad \text{and} \qquad F_s = q\frac{\rho_s^3}{3\varepsilon_0}\cdot r \quad (r < R_s) \qquad (4.3.2)$$

where q and r are the charge and the radial coordinate of ions.

The effect of the space charge was investigated by calculations with PISA-QMS. The mass spectra of 100-500u ions were simulated for various ion densities which are the space charge density themselves. In this simulation, the helium gas pressure was fixed to 1.0×10^{-4} Torr. The other parameters were the same as those listed in Table 4-3.

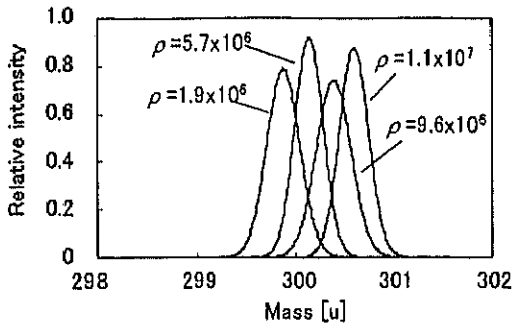

Fig.4-14 Simulated mass spectra of 300 *u* ions for different ion densities, ρ [/cm^3] .

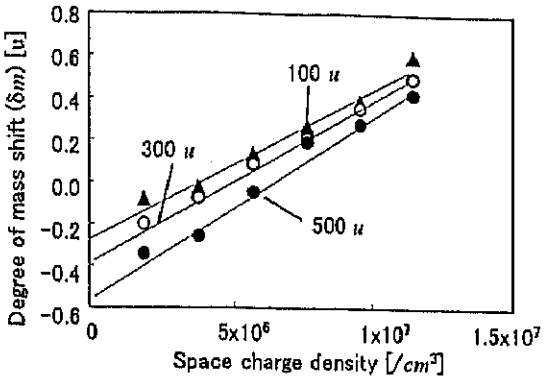

Fig.4-15 The influence of ion density on the degree of mass shift.

Typical mass spectra for 300u ions are shown in Fig.4-14. Basically the ion density in this region does not deteriorate the mass resolution significantly. However, Fig.4-15 indicates how the mass shift δm depends on the ion density. For all simulated ion masses the mass shift increases linearly with increased ion density. To make $|\delta m|$ lower than the maximum permissible value of 0.5, the ion density in ITMS should be maintained in the range from $\sim 3.0\times10^6$ to 1.0×10^7 [ions/cm^3].

The ion density confinable in ITMS had been estimated theoretically. Schwebel *et al.*[42] proposed a theoretical model in which the boundary of the stability region (in Fig.3-8(c)) is shifted due to the potential induced by the space charge. The relationship between the magnitude of the shift Δa_z or Δa_r and the maximum ion density ρ_{max} was reported as follows:

$$\Delta a_z = \frac{-32e\pi}{3m\Omega^2}\cdot\rho_{max} \qquad \text{and} \qquad \Delta a_r = \frac{-8e\pi}{3m\Omega^2}\cdot\rho_{max}\,.$$

The model of Schwebel *et al.* was confirmed experimentally by Todd *et al.*[43]. According to the above relation and the observed magnitude of the shift Δa_z or Δa_r, Fulford *et al.*[44] experimentally obtained the maximum ion density of 6.4×10^6 [ions/cm^3], that is within the

optimal range in Fig.4-15. Therefore, our results obtained from numerical simulations strongly support such theoretical and experimental results.